**Journal of Magnetics** 31(1), 1-13 (2026)

ISSN (Print) 1226-1750
ISSN (Online) 2233-6656
https://doi.org/10.4283/JMAG.2026.31.1.1

# Research on Torque Ripple Suppression of Halbach Array Machine Based on High-order Harmonic Cosine Function Magnet Pole Arc Trimming

**Xiaoxin Wu, Hui Wang, Haoen Xu, Chengyi Dao, and Junqiang Zheng***

*School of Electrical Engineering and Automation, Nantong University, Nantong 226019, China*

(Received 18 November 2025, Received in final form 8 January 2026, Accepted 16 January 2026)

**A new method that combines cosine pole arc trimming and high-order harmonics is proposed to address torque ripple issues in Halbach-array permanent magnet synchronous machines during high-performance operations. Tunable harmonic-modification functions are introduced at the edges of magnetic-pole slots based on a synergistic optimization strategy combining "multi-objective global optimization and local geometric modification" to effectively suppress torque ripple without significantly reducing the average torque. By focusing on a 9-slot, 6-pole Halbach machine, CHC-3, CHC-5, and CHC-7 schemes are designed and analyzed, and a cosine pole-arc contour modification equation is derived to parametrically describe the magnet's surface profile. Among the selected schemes, CHC-3 demonstrates highly effective torque ripple suppression by approximately 20–25%, decreasing the average torque by only about 1%.**

**Keywords :** Halbach-array, magnet pole arc trimming, cosine function, high-order harmonics, torque ripple

## 1. Introduction

Global energy crises and environmental issues have recently become increasingly prominent, pushing forward a rapid development of strategic emerging industries such as new energy vehicles, aerospace equipment, and high-end servo control systems [1-4], and imposing at the same time stricter demand on power and actuator systems, particularly in terms of high power density, efficiency, reliability, and smooth operation. Electric machines are central parts of energy conversion and power output devices, decisively determining their overall performance and competitiveness [5-7].

Halbach arrays (named after the physicist Klaus Halbach) were proposed to enable a strategic arrangement of magnetization directions, e.g., to enhance the magnetic field on one side of the air gap whilst substantially weakening it on the opposite side, effectively achieving a unidirectional magnetic field concentration effect [8]. Halbach arrays significantly improved energy efficiency in applications like coreless machines or magnetic levitation systems [9, 10].

Research on Halbach machines, i.e., electric devices that implement Halbach arrays, had sparked in Europe, the United States, and Japan, initially focusing on magnetic-field modeling and the experimental validation of Halbach permanent-magnet arrays, significantly advancing the current state-of-the-art. For instance, researchers at Lawrence Berkeley National Laboratory applied Halbach arrays to accelerators and magnetic levitation systems, demonstrating their unique ability to enhance magnetic fields in a specific, single direction [11, 12].

Various modification techniques of Halbach magnet arrays have been recently proposed worldwide to suppress torque ripple and reduce losses, including pole-arc trimming based on Fourier component optimization and the segmented magnet design based on multi-objective optimization.

Torque ripple in Halbach machines was extensively investigated due to its theoretical value and notable engineering significance. The performance metrics of PMVMs with a Halbach magnet array were studied for different slot/pole combinations and winding layouts (short pitch, fractional slot, and an odd number of slots or poles) [13]. A novel dual-magnetically-geared Halbach-array-based tubular linear permanent magnet generator (DMG-TLPMG) was developed for a direct-drive wave energy converter (DD-WEC) [14]. A novel bearing-less electromagnetic reaction wheel (ERW) design with a

---

*Corresponding author: Tel: +86-15190823468
e-mail: zjq@ntu.edu.cn

Halbach array coil configuration and ferrite cores was presented to overcome weak magnetic fields and start-up failures in current ERWs [15]. A shaping method with a variable rotor profile and pole arc span was established using Genetic Algorithm optimization [16]. Furthermore, an equivalent transformation approach for permanent-magnet (PM) electrical machines was presented using a coordinate transformation theory [17]. It was demonstrated that the aggregation of fluctuations in inductance, back electromotive force, and cogging torque contributes to increased torque ripple [18], while an asymmetric pole-shaping method was proposed to reduce torque ripple. A sensorless motor drive scheme was developed by fusing the electrical model-based estimation and the mechanical model-based observer with respect to the position servo with a heavy load [19]. Two novel hybrid interior permanent magnet synchronous machines (IPMSMs) that combine rare-earth PMs (RE-PMs) and ferrite PMs (FPMs) were reported to enhance the torque density and improve the PM utilization ratio [20].

Overall, significant progress has been made in theoretical modeling, finite element simulation, and engineering prototype design of Halbach machines. However, key challenges, including torque ripple, manufacturing processes, and high cost, are still not resolved, requiring timely further in-depth research.

Fig. 1 illustrates different magnetization methods of Halbach arrays. The unique distribution of the air-gap magnetic field in Halbach-array machines often results in a significant number of harmonic components in the air-gap magnetic flux density, which, in combination with stator slot effects, winding layout, and supply current harmonics, readily causes torque ripple during machine operation.

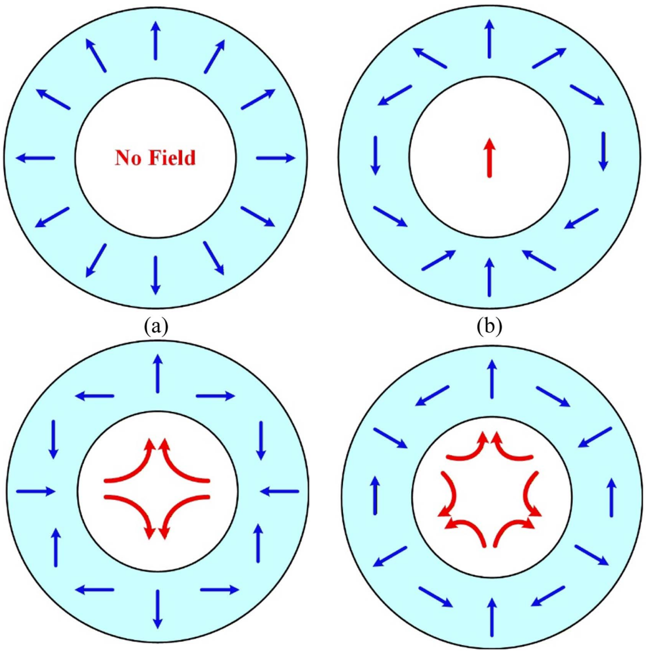

**Fig. 1.** (Color online) Halbach Arrays with Different Magnetization Methods: (a) k=1; (b) k=2; (c) k=3; (d) k=4.

To overcome the inherent limitations of conventional pole-arc trimming methods, the present study employs a cosine-based pole-arc trimming method and introduces 3rd-, 5th-, and 7th-harmonic components into the magnet pole-arc curve to compensate and generate three distinct cosine pole-arc trimming curves, designated as CHC-3, CHC-5, and CHC-7, respectively. A systematic analysis and optimization design focused on the torque ripple issue in Halbach machines is conducted by comparing the effects of these three cosine pole-arc trimming forms on the torque ripple reduction and the average torque.

The manuscript is structured as follows: In Chapter 2, the fundamental principles of Halbach machines are presented, along with an examination of their air gap magnetic flux characteristics. Chapter 3 elaborates in detail the collaborative optimization strategy of "multi-objective global optimization combined with local geometric commutation," accompanied by a comprehensive analysis of three distinct cosine pole commutation schemes (CHC-3, CHC-5, and CHC-7). Chapter 4 presents systematic simulation studies on these three schemes and comparatively analyzes and evaluates the experimental results. The Conclusion chapter summarizes the main findings of the study.

## 2. Air Gap Magnetic Flux Characteristics of Halbach Machines

### 2.1. Introduction and Fundamental Principles of Halbach Arrays

A standard configuration of a Halbach array is shown in Fig. 2. This magnetization pattern deviates from the conventional radial or tangential magnetization characteristic for traditional machines. Instead, this configuration of permanent magnets achieves "unidirectional field enhancement" through magnetization vectors that gradually rotate in space.

It can be regarded that an ideal Halbach magnet ring array exhibits a rotating magnetization distribution. The magnetization vector $M(\theta)$ is then:

$$M(\theta) = M_0[\cos(p\theta)\hat{r} + \sin(p\theta)\hat{\theta}] \tag{1}$$

where $M_0$ represents the magnetization amplitude, $\theta$ denotes the electrical angle, and $p$ indicates the number of pole pairs. Such a magnetization distribution effectively

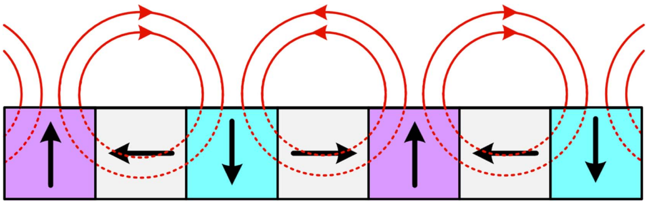

**Fig. 2.** (Color online) Halbach array structure comprising two sets of permanent magnets per pole.

forms a self-sustaining current loop within the magnet array, enhancing the strength of the magnetic field on the air-gap side while suppressing it on the back-iron side, significantly improving the magnet's utilization efficiency.

Based on the magnetization vector's distribution, the equivalent magnetizing current density is:

$$J_m = \nabla \times M \tag{2}$$

By substituting Eq. (2) into Eq. (1), the harmonic expansion of the air gap magnetic field is obtained:

$$B_r(r,\theta) = \sum_{m=1,3,5,\ \ldots} B_m \cos(m\theta) \tag{3}$$

$$B_\theta(r,\theta) = \sum_{m=1,3,5,\ \ldots} B_m \sin(m\theta) \tag{4}$$

where the fundamental wave amplitude can be expressed as:

$$B_1 = \frac{B_r}{1+(\mu_r-1)\dfrac{g}{h_{PM}}} \tag{5}$$

where $B_r$ is the remanent magnetization of the magnet, $g$ is the equivalent air gap, and $h_{PM}$ is the magnet thickness. Thus, Halbach arrays can give higher air gap fundamental wave densities at the same thickness.

### 2.2. The Spatial Distribution of the Magnetic Flux Density in the Air Gap

For a high-permeability stator and rotor cores ($\mu_r \rightarrow \infty$), where the air gap magnetic field satisfies the Laplace equation, the "magnetic potential-air gap magnetic flux density" convolution model is commonly used:

$$B_r(\theta) = \mu_0 \Lambda(\theta) \star F(\theta) \tag{6}$$

$$F(\theta) = F_{pm}(\theta) + F_w(\theta) \tag{7}$$

where $B_r(\theta)$ represents the spatial distribution of the radial magnetic flux density in the air gap, varying with the mechanical angle $\theta$; $\mu_r$ is the vacuum permeability, $\Lambda(\theta)$ is the air gap permeability, and $F(\theta)$ is the circumferentially distributed magnetic motive force (MMF); $F_{pm}(\theta)$ is the magnetic motive force distribution provided by the permanent magnet, and $F_w(\theta)$ is the magnetic motive force generated by the winding current.

Under ideal, $\Lambda(\theta) = \Lambda_0 = 1/g_{eq}$, and no-load, $F(\theta) \approx F_{pm}(\theta)$, conditions, the spatial distribution of the radial magnetic flux density is as follows:

$$B_r(\theta) = \mu_0 \Lambda_0 F_{pm}(\theta) \tag{8}$$

where $g_{eq}$ represents the equivalent air gap.

The relationship between the equivalent air gap and the mechanical air gap is:

$$g_{eq} = k_C g \tag{9}$$

where $k_c$ is the Carter coefficient, which can be approximated as follows:

$$k_C = \frac{\tau_s}{\tau_s - \Upsilon g} \tag{10}$$

When $k_c > 1$, the equivalent air gap is amplified, the average magnetic flux decreases, and the magnetic flux density, $B_0$, within the pole piece is reduced.

Fig. 3 illustrates a simplified air gap and magnet model used to explain the generation of the air gap magnetic flux density. For a synchronous machine with a surface-mounted permanent magnet with a thickness $h_{PM}$ and a relative permeability $\mu_{mr}$ of ~1.05, $B_o$ under the one-dimensional equivalent magnetic circuit approximation is:

$$B_0 = \frac{B_r \dfrac{h_{PM}}{\mu_{mr}}}{g_{eq} + \dfrac{h_{PM}}{\mu_{mr}}} \tag{11}$$

Let the pole arc coefficient $\alpha$ be $\beta/\tau_p \in (0,1]$, where $\beta$ is the permanent magnet pole arc, and $\tau_p$ is the pole pitch; under ideal conditions, $B_r(\theta)$ contains only odd-order harmonics:

$$B_r(\theta) = m = \sum_{m=1}^{\infty} \hat{B}_{(2m-1)} cos((2m-1)p\theta) \tag{12}$$

$$\hat{B}_{(2m-1)} = B_0 \cdot C_{(2m-1)}(\alpha) \cdot k_{(2m-1)} \tag{13}$$

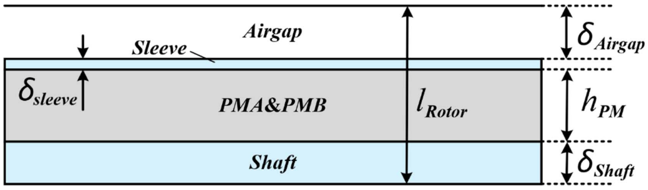

**Fig. 3.** (Color online) Simplified air-gap and the PM model to explain air-gap flux density production.

$$C_{(2m-1)}(\alpha) = \frac{4}{(2m-1)\pi}\sin\left(\frac{(2m-1)\pi a}{2}\right) \tag{14}$$

The left side of Eq. (13) represents the amplitude of the $(2m-1)^{\text{th}}$ odd-order pole-pole harmonic; $k_{(2\text{m}-1)}$ denotes the geometric attenuation coefficient, where higher-order harmonics attenuate more rapidly in the air gap; $c_{(2\text{m}-1)}(\alpha)$ signifies the pole arc-induced sinc envelope.

### 2.3. The Spatial Modulation of Air Gap Permeability

Slotting induces periodic fluctuations in the air gap magnetic flux density (with the fundamental frequency determined by the number of slots $Z_s$), which can be expressed as follows:

$$\Lambda(\theta) = \Lambda_0\left[1 + \sum_{n=1}^{\infty}\lambda_n\cos(nZ_s\theta + \phi_n)\right] \tag{15}$$

where $\Lambda_0 = 1/g_{eq}$ represents the average magnetic permeability corresponding to the equivalent air gap, while $\lambda_n$ denotes the amplitude coefficient of the n$^{\text{th}}$ magnetic fluctuation.

The modulation of the magnetic flux generates sidebands for the intrinsic polar pair harmonic $(2m-1)$:

$$(2m-1)p \to (2m-1)p \pm nZ_s \quad (n = 1, 2, \ldots) \tag{16}$$

The left-hand side of Eq. (16) represents the order in the original space, while its right-hand side denotes the order in the sideband space.

The amplitude of the sideband is approximately proportional to the first-order modulation coefficient under the small-signal approximation, $\lambda_n$, which not only alters the peaks and troughs of the $B_r(\theta)$ waveform but also directly impacts the cogging torque, electromagnetic noise, and counter-electromotive force.

$$\hat{B}^{(\pm)}_{(2m-1),n} \approx \frac{\lambda_n}{2}\hat{B}^{(0)}_{(2m-1)} \tag{17}$$

$$\hat{B}^{(0)}_{(2m-1)} = B_0 C_{(2m-1)}(\alpha) k_{(2m-1)} \tag{18}$$

The left-hand side of Eq. (17) represents the positive/negative sideband amplitude generated by the $(2m-1)$ odd-order pole pair harmonic from the $n^{\text{th}}$ magnetic flux fluctuation.

The finite stack length causes the axial attenuation of the air gap field. The end coefficient, $k_{\text{end}}$, is commonly used to correct the fundamental wave amplitude. Overall, these effects can be combined as the following coefficient:

$$\hat{B}_{(2m-1)} \to \hat{B}_{(2m-1)} \cdot k_{end} \cdot k_{leak} \tag{19}$$

$k_{\text{end}}$ accounts for the axial attenuation and the end leakage magnetic flux caused by the finite stack length, typically less than 1; $k_{\text{leak}}$ is the leakage correction coefficient.

In summary, the radial air gap magnetic flux density ($r = R_g$) can be expressed as follows:

$$\begin{aligned} B_r(\theta) \approx {} & \sum_{m=1}^{\infty}\left[\hat{B}^{(0)}_{(2m-1)}\cos\left((2m-1)p\theta\right)\right] \\ & + \sum_{m=1}^{\infty}\sum_{n=1}^{\infty}\left[\hat{B}^{(0)}_{(2m-1),n}\cos\left(\left((2m-1)p \pm nZ_s\right)\theta + \varphi_{mn}\right)\right] \end{aligned} \tag{20}$$

where

$$\hat{B}^{(0)}_{(2m-1)} = B_0 \cdot C_{(2m-1)}(\alpha) \cdot k_{(2m-1)} \cdot k_{end} \cdot k_{leak} \tag{21}$$

$$\hat{B}^{(\pm)}_{(2m-1),n} = \frac{\lambda_n}{2}\hat{B}^{(0)}_{(2m-1)} \tag{22}$$

In the air gap radial magnetic field of a surface-mounted permanent magnet machine under ideal slotless conditions, the magnetic field consists of odd-order pole pair harmonics, whose amplitude is determined by the pole-arc ratio's sinc envelope and the equivalent air gap. However, when considering slotting, end-winding effects, eccentricity, and saturation, the spatial modulation of the magnetic flux density generates sidebands spaced by the number of slots, significantly altering the spatial distribution of $B_r(\theta)$ and its electromagnetic performance.

## 3. A Collaborative Optimization Strategy Combining Multi-Objective Global Optimization and Local Geometric Modifications

In this study, we propose a collaborative optimization strategy that combines global multi-objective optimization with local geometric modifications to address torque ripple suppression in Halbach permanent magnet machines. First, a global parametric model that incorporates key parameters, such as Halbach motor dimensions and the pole arc coefficient, is established. The model prioritizes torque ripple minimization as the primary objective while ensuring the output torque, and simultaneously optimizes the permanent magnet's volume to enhance the cost efficiency. A multi-objective optimization algorithm is employed to identify the Pareto front. Then, building on this global optimization, a local geometric modification of rotor poles is introduced to specifically suppress the torque ripple of specific orders caused by magnetic-circuit saturation and back-EMF harmonics. The global optimization ensures the overall optimal balance between the motor's macro performance and material costs, while the local shaping further suppresses torque ripple. The synergy of both global and local strategic segments pushes the envelope of the torque ripple optimization while strictly guaranteeing the output torque, balancing the economic efficiency and maximizing the efficient utilization of permanent magnet materials.

### 3.1. Multi-Objective Global Optimization

A 9-slot 6-pole Halbach array machine was selected to investigate the effect of cosine pole-arc trimming with high-order harmonic injection on reducing torque ripple. Fig. 4(a) illustrates the stator and winding structure of the 9-slot 6-pole Halbach array machine; Fig. 4(b) depicts the magnet structure, including the air gap side sheath, Halbach magnet array, and rotor shaft, where the Halbach magnet array and the rotor shaft are configured to cooperate. Fig. 4(b) also illustrates the magnet assembly of the 9-slot, 6-pole Halbach machine, comprising two sets of permanent magnets with mutually orthogonal magnetization directions. Some permanent magnets (PMA) employ radial magnetization, while others (PMB) utilize parallel magnetization. PMA and PMB magnets are alternately arranged in a circumferential pattern, and their 90° spatial magnetization angle forms a classic Halbach array, enhancing the magnetic field on the air gap side while canceling the magnetic flux on the back side. This configuration improves the utilization of magnetic energy and boosts the machine's output performance. PMA and PMB are made of neodymium-iron-boron, while the air gap side sheath and inner shaft sections are manufactured from austenitic heat-resistant stainless steel.

The optimization strategy first requires optimizing the key design parameters of the 9-slot, 6-pole Halbach array machine. Traditional single-objective optimization approaches struggle to balance complex constraints across different performance metrics; hence, multi-objective optimization based on evolutionary algorithms like multi-objective Genetic Algorithm and Random-search. All optimized parameters for the stator, rotor, and permanent magnets are listed in Table 1. Fig. 5 shows the Pareto front diagram obtained through the multi-objective optimization, in which the torque ripple optimization is prioritized to reduce it to within 10%. Under this premise, the output torque should be maximized. The optimized machine parameters and changes in the output torque and torque ripple are given in Table 2.

However, even after the optimal parameter combination is obtained via multi-objective optimization, residual torque ripple remains difficult to eliminate due to slot effects, magnetic circuit nonlinearity, and harmonic coupling, affecting the air gap magnetic field distribution.

**Table 1.** Optimized machine machine key design specifications and parameters.

| Design parameters | 9-Slot/6-Pole | |
|---|---|---|
| Slot number | 9 | - |
| Pole number | 6 | - |
| Rated speed | 25000 | rpm |
| Peak current | 14 | A |
| Stator outer diameter | 84 | mm |
| Stator inner-to-outer diameter ratio | 36/84 | - |
| Axial length | 55 | mm |
| Turns in series per phase | 17 | - |
| Tooth width | 6.3 | mm |
| Back-iron | 7.4 | mm |
| Slot opening | 2.2 | mm |
| Slot opening height | 0.6 | mm |
| Upper Slot opening height | 0.4 | mm |
| Minimum airgap length | 0.8 | mm |
| Pole arc coefficient | 0.5 | - |
| Maximun PMA thickness | 5.5 | mm |
| Maximun PMB thickness | 4.9 | mm |

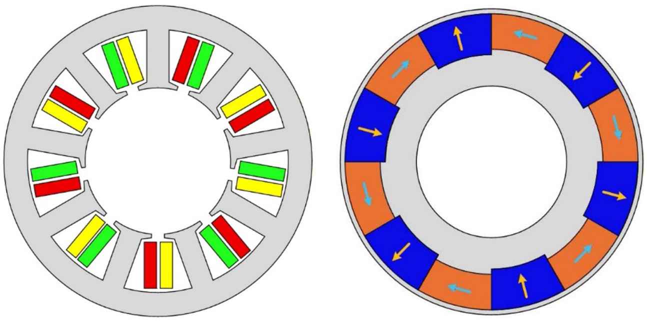
(a) (b)

**Fig. 4.** (Color online) Topology of a 9-slot 6-pole Halbach machine: (a) 9-slot stator; (b) 6-pole rotor with Halbach magnet configuration.

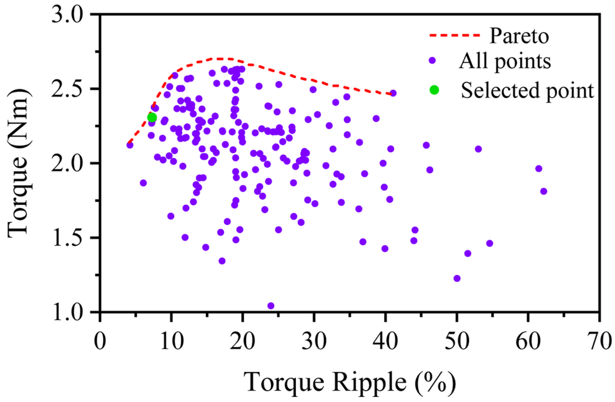

**Fig. 5.** (Color online) The Pareto front diagram obtained through multi-objective optimization.

**Table 2.** Comparison of key parameters before and after optimization.

| Optimized parameters | Original | Optimized |
|---|---|---|
| Pole arc coefficient | 0.5 | 0.5 |
| Maximun PMA thickness(mm) | 4.4 | 5.5 |
| Maximun PMB thickness(mm) | 4 | 4.9 |
| Slot opening height(mm) | 0.6 | 0.5 |
| Upper Slot opening height(mm) | 0.4 | 0.3 |
| Slot opening(mm) | 1.8 | 2.2 |
| Tooth width(mm) | 8.5 | 6.3 |
| Average torque(Nm) | 2.2 | 2.3 |
| Torque ripple (%) | 24.3 | 7.3 |

To further mitigate fluctuations of residual electromagnetic torque upon the optimization, magnet pole-arc trimming is applied as an effective secondary optimization method.

As shown in Fig. 6, the following section systematically addresses the impact of pole arc trimming on the electromagnetic performance of electric machines by introducing adjustable curve functions at the edges of magnet pole arcs. Specifically, a cosine-based pole arc trimming method (Cosine Harmonic Collaboration Trimming, CHC) is applied in this work. 3rd-, 5th-, and 7th-order harmonic components are respectively injected into the magnet pole arc curve to form three distinct cosine pole arc trimming curves, denoted as CHC-3, CHC-5, and CHC-7, respectively. The torque ripple suppression and average torque effects of these cosine pole-arc trimming forms are compared and used to systematically analyze and optimize the design of the Halbach machine's torque ripple issues. The effectiveness of the proposed cosine pole-arc trimming forms in suppressing torque ripple, maintaining output torque, and achieving a performance-complexity balance is assessed, thereby balancing engineering demand and performance enhancement.

### 3.2. Cosine pole arc trimming with the 3rd harmonic (CHC-3)

In this study, the pole arc coefficient, $em_A$, of the investigated Halbach machine, represents the relative proportion of the magnetic pole arc within the pole pitch and serves as a key geometric parameter that determines the air gap magnetic flux density waveform and electromagnetic torque characteristics of the machine. The magnet assembly of the Halbach machine consists of two sets of permanent magnet blocks, PMA and PMB, with mutually orthogonal magnetization directions, forming a typical Halbach magnetization array structure with a 90° spatial magnetization angle difference.

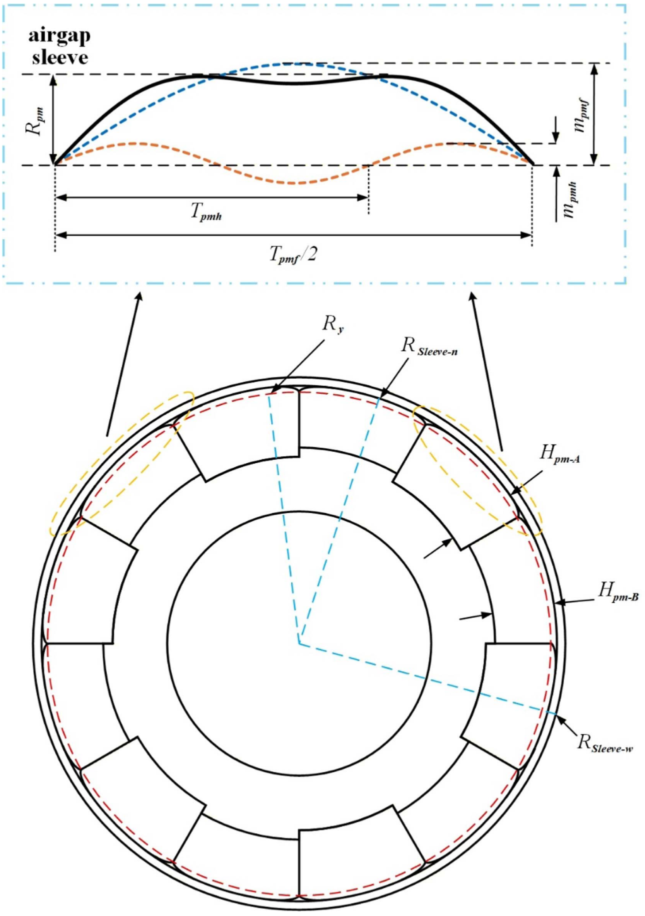

**Fig. 6.** (Color online) Cosine pole arc trimmed structure collaborated with high-order harmonic of Halbach Array Permanent Magnet.

The original thicknesses of PMA and PMB before pole arc trimming in the designed Halbach array machine are defined as $H_{pm-A}$ and $H_{pm-B}$, respectively, both representing radial thicknesses. The inner diameter of the machine's sleeve, $R_{sleeve-n}$, determines the mechanical constraints on the outer circumference of the machine's rotor and the boundary for magnet placement.

To effectively reduce torque ripple in Halbach machines while minimizing loss of the average output torque, we employ the same cosine pole-arc trimming method, combined with higher-order harmonics, for both PMA and PMB permanent magnets. The core principle of this pole-arc shaping strategy is to preserve the fundamental wave distribution of the magnets while appropriately introducing specific harmonic components (herein, tertiary harmonics). This optimizes the air gap magnetic flux waveform via spatial harmonic interference, thereby achieving smoother torque waveforms.

The profile curve is based on the expansion of the cosine function, with the fundamental wave corresponding to the magnet's original arc-shaped contour; higher harmonics are used to fine-tune the magnet's surface shape. The fundamental wave amplitudes of PMA's and PMB's profile curves are defined as $m_{pmf\text{-}A}$ and $m_{pmf\text{-}B}$, while the 3rd harmonic amplitudes are $m_{pmh\text{-}A}$ and $m_{pmh\text{-}B}$, respectively. The radius of the concentric circle in the machine where the trim curve reference line (y-axis) lies is denoted as $R_y$, and it is located near the magnet's neutral layer and defines the geometric center of the trim curve.

The primary amplitude ratio parameters in this study are determined as follows:

$$\frac{m_{pmf-A}}{m_{pmh-A}} = 8.9 \quad , \quad \frac{m_{pmf-B}}{m_{pmh-B}} = 8.4 \tag{23}$$

The amplitude ratio of the 3rd harmonic and the fundamental wave is ~11%, effectively reducing the distortion rate of the air gap magnetic flux density without significantly weakening the fundamental wave's magnetic field strength. At the same time,

$$R_{sleeve-n} - R_y = R_{pm} \tag{24}$$

$$\frac{R_{pm}}{R_{sleeve-n}} = 0.016 \tag{25}$$

The above equations indicate that the shaping depth is approximately 1.6% of the sheath radius, falling within the range of minor shaping. This approach balances manufacturing feasibility with the magnetic field optimization. All design parameters and geometric dimensions are shown in detail in Fig. 6.

The pole number of the Halbach machine is set to 2$P$ in the spatial angle. For each pole pair, the fundamental periodicity of the modified curve for PMA and PMB is defined as $T_{pmf\text{-}A}$ and $T_{pmf\text{-}B}$, while the corresponding 3rd harmonic periodicity is defined as $T_{pmh\text{-}A}$ and $T_{pmh\text{-}B}$, respectively. Fig. 7(a) illustrates the specific structural parameters and modification curves of the cosine pole-arc trimming structure with the injected 3rd harmonic. The adjustable curve functions for the pole-arc trimming of PMA and PMB magnets can be expressed as follows:

$$y_{PMA} = m_{pmf-A}\cos\left(\frac{2\pi}{T_{pmf-A}}x\right) - m_{pmh-A}\cos\left(\frac{2\pi}{T_{pmh-A}}x\right) + \frac{R_y}{\sqrt{1+\tan^2\left(\frac{\pi}{2P}\cdot em_A\right)}} \tag{26}$$

$$y_{PMB} = m_{pmf-B}\cos\left(\frac{2\pi}{T_{pmf-B}}x\right) - m_{pmh-B}\cos\left(\frac{2\pi}{T_{pmh-B}}x\right) + \frac{R_y}{\sqrt{1+\tan^2\left(\frac{\pi}{2P}\cdot(1-em_A)\right)}} \tag{27}$$

where

$$T_{pmf-A} = \frac{4\cdot R_y}{\sqrt{1+\cot^2\left(\frac{\pi}{2P}\cdot em_A\right)}} \tag{28}$$

$$T_{pmf-B} = \frac{4\cdot R_y}{\sqrt{1+\cot^2\left(\frac{\pi}{2P}\cdot(1-em_A)\right)}} \tag{29}$$

$$\frac{T_{pmf-A}}{T_{pmh-A}} = \frac{T_{pmf-B}}{T_{pmh-B}} = 3 \tag{30}$$

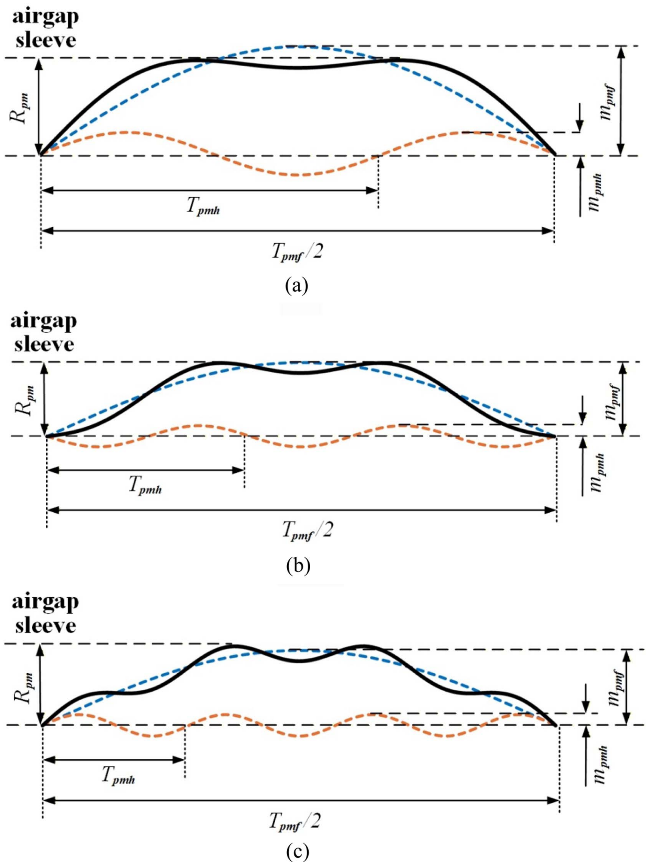

**Fig. 7.** (Color online) Cosine pole arc trimmed structure collaborated with high-order harmonic: (a)CHC-3; (b) CHC-5; (c)CHC-7.

### 3.3. Cosine pole arc trimming with the 5th harmonic (CHC-5)

Building upon the elaboration of CHC-3, this section further investigates the effects of cosine-polar arc trimming in combination with the 5th harmonic on the air gap magnetic flux density and electromagnetic torque characteristics of the studied Halbach machine.

Similar to the aforementioned 3rd-harmonic rectification, the cosine polar arc rectification with the 5th-harmonic injection is also based on the fundamental cosine distribution. However, it superimposes a cosine component onto the rectification curve at five times the fundamental frequency.

Fig. 7(b) shows the specific structural parameters of CHC-5, along with modification curves. The adjustable curve functions for the pole-arc trimming of PMA and PMB magnets can be expressed as follows:

$$y_{PMA\text{-}5} = m_{pmf5-A}\cos\left(\frac{2\pi}{T_{pmf5-A}}x\right) - m_{pmh5-A}\cos\left(\frac{2\pi}{T_{pmh5-A}}x\right) + \frac{R_y}{\sqrt{1+\tan^2\left(\frac{\pi}{2P}\cdot em_A\right)}} \tag{31}$$

$$y_{PMB\text{-}5} = m_{pmf5-B}\cos\left(\frac{2\pi}{T_{pmf5-B}}x\right) - m_{pmh5-B}\cos\left(\frac{2\pi}{T_{pmh5-B}}x\right) + \frac{R_y}{\sqrt{1+\tan^2\left(\frac{\pi}{2P}\cdot(1-em_A)\right)}} \tag{32}$$

where

$$T_{pmf-A} = \frac{4\cdot R_y}{\sqrt{1+\cot^2\left(\frac{\pi}{2P}\cdot em_A\right)}} \tag{33}$$

$$T_{pmf-B} = \frac{4\cdot R_y}{\sqrt{1+\cot^2\left(\frac{\pi}{2P}\cdot(1-em_A)\right)}} \tag{34}$$

$$\frac{T_{pmf5-A}}{T_{pmh5-A}} = \frac{T_{pmf5-B}}{T_{pmh5-B}} = 5 \tag{35}$$

where $m_{pmf5\text{-}A}$ and $m_{pmf5\text{-}B}$ represent the modified fundamental wave amplitudes, while $m_{pmh5\text{-}A}$ and $m_{pmh5\text{-}B}$ denote the amplitudes of the modified 5th harmonic, respectively.

To avoid excessive contouring that may lead to complex machining and magnet stress concentration, the amplitude ratio between the fundamental wave and the 5th harmonic is maintained within a reasonable range. After multiple rounds of parameter comparison and optimization, the amplitude ratios are determined as follows:

$$\frac{m_{pmf5-A}}{m_{pmh5-A}} = 4.8 \quad , \quad \frac{m_{pmf5-B}}{m_{pmh5-B}} = 4.3 \tag{36}$$

The amplitude of the 5th harmonic accounts for ~21 to 23% of the fundamental wave amplitude. The radius of the concentric circle where the reference line of the modified curve (y-axis) is located is set as *Ry*, with the corresponding relationship:

$$R_y = R_{sleeve-n} \tag{37}$$

This ensures that the number of used permanent magnets is not significantly reduced during pole-arc trimming, thereby suppressing torque ripple while minimizing the output torque loss.

### 3.4. Cosine pole arc trimming with the 7th harmonic (CHC-7)

Following the study of CHC-3 and CHC-5 designs, this section further proposes a cosine-polar arc trimming design with the 7th-harmonic to explore additional possibilities for higher-order harmonics in the Halbach machine's magnet pole modification.

Fig. 7(c) shows the specific structural parameters and correction curves for the cosine pole-arc correction structure with the 7th-harmonic injection. The adjustable pole-arc correction curve functions for PMA and PMB are expressed as follows:

$$y_{PMA\text{-}7} = m_{pmf7-A}\cos\left(\frac{2\pi}{T_{pmf7-A}}x\right) - m_{pmh7-A}\cos\left(\frac{2\pi}{T_{pmh7-A}}x\right) + \frac{R_y}{\sqrt{1+\tan^2\left(\frac{\pi}{2P}\cdot em_A\right)}} \tag{38}$$

$$y_{PMB\text{-}7} = m_{pmf7-B}\cos\left(\frac{2\pi}{T_{pmf7-B}}x\right) - m_{pmh7-B}\cos\left(\frac{2\pi}{T_{pmh7-B}}x\right) + \frac{R_y}{\sqrt{1+\tan^2\left(\frac{\pi}{2P}\cdot(1-em_A)\right)}} \tag{39}$$

where

$$T_{pmf-A} = \frac{4\cdot R_y}{\sqrt{1+\cot^2\left(\frac{\pi}{2P}\cdot em_A\right)}} \tag{40}$$

$$T_{pmf-B} = \frac{4 \cdot R_y}{\sqrt{1+\cot^2\left(\frac{\pi}{2P}\cdot\left(1-em_A\right)\right)}} \tag{41}$$

$$\frac{T_{pmf7-A}}{T_{pmh7-A}} = \frac{T_{pmf7-B}}{T_{pmh7-B}} = 7 \tag{42}$$

$m_{pmf7\text{-}A}$ and $m_{pmf7\text{-}B}$ denote the modified fundamental wave amplitudes, while $m_{pmh7\text{-}A}$ and $m_{pmh7\text{-}B}$ represent the corresponding modified 7th harmonic amplitudes, respectively. Due to the higher frequency of the 7th harmonic, more subtle peaks and troughs are introduced within a single pole range, further refining periodic disturbance characteristics on the magnet's surface.

To avoid excessive contouring that may lead to complex machining and magnet stress concentration, the amplitude ratio between the fundamental wave and the 7th harmonic is retained within a reasonable range. After multiple rounds of parameter comparison and optimization, the amplitude ratios are determined as follows:

$$\frac{m_{pmf7-A}}{m_{pmh7-A}} = 12 \quad , \quad \frac{m_{pmf7-B}}{m_{pmh7-B}} = 10.6 \tag{43}$$

The amplitude of the 7th harmonic is only ~8.3 to 9.4% of the fundamental wave. The profile reference radius is defined as $R_y$ and satisfies the following relationships:

$$R_{sleeve-n} - R_y = R_{pm} \tag{44}$$

$$\frac{R_{pm}}{R_{sleeve-n}} = 0.003 \tag{45}$$

During pole-arc trimming with the 7th-harmonic injection, the utilization of the permanent magnet is maintained at a nearly constant level, effectively suppressing torque ripple while minimizing the output torque loss.

### 3.5. Application extension of cosine pole-arc trimming with high-order harmonics

The cosine pole-arc trimming with high-order harmonics, originally developed here for Halbach machines, can also be adapted for conventional surface-mounted permanent magnet synchronous machines (SPMSMs). Traditional radially magnetized SPMSMs feature simple structures, straightforward manufacturing, and low costs, making them the mainstream solution for industrial applications. Therefore, adapting and extending the developed method of cosine pole-arc trimming with high-order harmonics to conventional SPMSMs has great theoretical and engineering value, not only to enrich the performance optimization toolkit for standard SPMSMs but also to provide a new design pathway toward high-performance, low-cost permanent magnet machines.

In SPMSMs, the original thickness of magnets before pole arc trimming is defined as $H_{pm\text{-}S}$, representing the radial thickness. The inner diameter of the machine's sleeve is denoted as $R_{sleeve\text{-}n}$, and it determines the mechanical constraints on the outer circumference of the machine's rotor and the boundary for magnet placement.

Similar to the Halbach machine, the profile curve is based on the expansion of a cosine function, with the fundamental wave corresponding to the magnet's original arc-shaped contour, and higher harmonics are used to fine-tune the magnet's surface shape. The fundamental wave amplitude of the profile curve is $m_{pmf\text{-}S}$, while the high-order harmonic amplitude is $m_{pmh\text{-}S}$. The radius of the concentric circle in the machine where the reference line of the trim curve (y-axis) is positioned is denoted as $R_{y\text{-}S}$; it is located near the magnet's neutral layer and defines the geometric center of the trim curve. The pole number of the SPMSM is set to $2P$ in the spatial angle. For each pole pair, the fundamental periodicity of the modified curve for the magnet is defined as $T_{pmf\text{-}S}$, while the higher-order harmonic periodicity is defined as $T_{pmh\text{-}S}$.

The adjustable curve functions for the pole-arc trimming of SPMSM magnets can be expressed as follows:

$$y_{SPMSM} = m_{pmf-S}\cos\left(\frac{2\pi}{T_{pmf-S}}x\right) - m_{pmh-S}\cos\left(\frac{2\pi}{T_{pmh-S}}x\right) + \frac{R_{y-S}}{\sqrt{1+\tan^2\left(\frac{\pi}{2P}\right)}} \tag{46}$$

where

$$T_{pmf-S} = \frac{4 \cdot R_{y-S}}{\sqrt{1+\cot^2\left(\frac{\pi}{2P}\right)}} \tag{47}$$

$$\frac{T_{pmf-A}}{T_{pmh-A}} = \frac{T_{pmf-B}}{T_{pmh-B}} = k \tag{48}$$

Here, k denotes the order of the higher harmonic.

## 4. Finite Element Modelling (FEM) and Experimental Results

Vast amounts of finite element simulation data are generated during parametric modeling and optimization, including air gap magnetic flux waveforms, back EMF, torque, and other parameters across different combinations of modification parameters. These data may include issues like numerical noise, outliers (quasi-missing data) caused by improper mesh partitioning or solution settings, and uncovered parameter space (active missing data). Several groups of data with questionable validity are presented below.

First, parametric scanning and sampling. Optimization algorithms generate a series of sample points within the design variable space. To ensure data quality and optimization efficiency, the sampling strategy requires an appropriate densification near variable boundaries and in regions likely to contain optimal solutions.

Second, anomaly identification and rejection in simulation results. Due to numerical instability in finite element solutions (e.g., severe mesh distortion or non-convergence of nonlinear iterations), individual sample points may yield physically unreasonable and anomalous data points (e.g., extremely negative torque values or abrupt changes in magnetic flux). During preprocessing, validity thresholds (e.g., average torque > 0 or local magnetic flux density below demagnetization threshold) should be established to automatically identify and flag such points as "invalid data", followed by their exclusion from subsequent optimization analyses or triggering the re-simulation of the sample point.

Third, noise smoothing processing. Transient waveforms (e.g., instantaneous torque) obtained from FEA calculations typically contain high-frequency numerical noise from time-step and spatial mesh discretization and/or solver residual errors. Tooth-slot torque calculations are particularly susceptible to this effect. For quantities requiring analysis of periodic ripple (e.g., torque pulsation), it is critical to apply periodicity-based smoothing techniques that align and average transient torque waveforms across multiple electrical cycles, effectively suppressing random numerical noise while highlighting periodic torque ripple components. After applying a Fast Fourier Transform (FFT) to the waveform, a reasonable cutoff frequency is set to filter out high-frequency components significantly above the electrical frequency (typically numerical noise); then, an inverse transform is applied to obtain the smoothed time-domain waveform. Nevertheless, filtering out genuine mechanical or electromagnetic harmonics must be avoided. For spatial waveforms such as air gap magnetic flux density distributions, Fourier series fitting can be used to extract harmonic coefficients up to a specified order (e.g., the first 20 harmonics), serving as an inherent noise reduction process that extracts key information from noisy data.

Finally, strategies for addressing "missing data" are required. When constructing optimization surrogate models (e.g., response surfaces or Kriging models), the simulation performance at active missing data (unsimulated points) must be predicted. This is achieved using the surrogate model itself, which essentially interpolates or regresses the design space based on the known sample points. For passive missing data (failed simulation points), e.g., the aforementioned outliers, handling approaches include: a) Ignoring and deleting failed data points if they are sparse and randomly distributed; b) Model repair utilizing the data from adjacent successful sample points to interpolate the approximate output value of the missing point. This procedure requires extreme caution and must be explicitly annotated.

To quantify the correction effect, the air gap magnetic flux Total Harmonic Distortion (THD) that defines how much the actual waveform deviates from a sine wave is defined as follows:

$$THD = \frac{\sqrt{\sum_{n=2}^{N} m_{pmh-n}}}{m_{pmf}} \tag{49}$$

where $m_{pmh\text{-}n}$ represents the amplitude of the n$^{th}$ harmonic, and $m_{pmf}$ denotes the fundamental wave amplitude. Compared to the CHC-5 and CHC-T schemes that inject the 5$^{th}$ harmonic and the 7$^{th}$ harmonic, respectively, the CHC-3 scheme (which injects the 3$^{rd}$ harmonic) achieves a more significant THD reduction. This demonstrates that a moderate introduction of cosine-polar arc modulation with the 3$^{rd}$-harmonic injection is more advantageous for harmonic suppression.

Fig. 8 shows the output torque waveforms of the Halbach machine employing the above*-mentioned different pole arc trimming structures. The bold blue, bold red, green, and gray curves show the output torque waveforms of the untrimmed original Halbach machine model, and the Halbach machine with cosine pole arc trimming structures with the injected 3$^{rd}$, 5$^{th}$, and 7$^{th}$ harmonics, respectively. The Halbach machine with the cosine pole-arc trimming structure incorporating the injected 3$^{rd}$ harmonic achieves a smoother output torque waveform, demonstrating the most effective suppression of torque ripple.

$$TRR = \frac{T_{max} - T_{min}}{T_{avg}} \times 100\% \tag{50}$$

$T_{max}$, $T_{min}$, and $T_{avg}$ represent the maximum, minimum, and average values of the electromagnetic torque, respec-

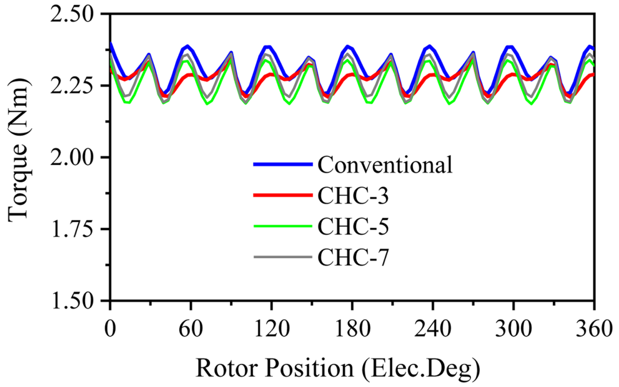

**Fig. 8.** (Color online) Comparison of output torque waveforms in Halbach machines with different pole arc trimming structures.

**Table 3.** Effects of various modification schemes on torque and ripple.

| Various schemes | Torque(Nm) | Effect | Ripple | Effect |
|---|---|---|---|---|
| Conventional Halbach | 2.31 | - | 7.30% | - |
| CHC-3 Scheme | 2.27 | -1.54% | 5.79% | -20.66% |
| CHC-5 Scheme | 2.26 | -2.17% | 6.89% | -5.62% |
| CHC-7 Scheme | 2.28 | -1.34% | 7.43% | +1.86% |

tively.

The calculation results are listed in Table 3. Under identical operating conditions, the torque ripple reduction (TRR) of the untrimmed model is ~7.30%, while the CHC-3 scheme achieves ~5.79%, representing a reduction of about 20.66%, representing the most effective TRR among the three trimming schemes. This result fully validates the effectiveness of the cosine trimming with the 3rd harmonic injection in mitigating torque ripple. Notably, the average torque $T_{avg}$ exhibits minimal variations, decreasing by only about 1.54%, indicating that the modification does not significantly impair the torque output.

Figs. 9 and 10 show the no-load back-EMF waveforms and cogging torque waveforms of the original model and the three different modification schemes. Simulation analysis indicates the virtually unchanged fundamental amplitude of the no-load back-EMF before and after the modification, with highly overlapping four waveforms, demonstrating that the adopted modification method effectively maintains the fundamental component of the air gap magnetic field while suppressing specific harmonics, thereby ensuring the motor's core power output capability.

Significant differences in cogging torque emerge among different harmonic injection schemes. The 3rd-harmonic injection yields the most ideal modification effect; the cogging torque waveform becomes exceptionally smooth during odd-numbered cycles and exhibits a marked amplitude reduction. This primarily occurs because the 3rd-harmonic magnetic field effectively cancels out the primary low-order magnetic flux harmonics introduced by stator cogging, thereby mitigating torque pulsations caused by reluctance variations. In contrast, the smoothing schemes with injected 5th- and 7th-harmonics show no noticeable improvement in the ripple torque waveform, the amplitudes of which even slightly increase, indicating that the 5th- and 7th-harmonic magnetic fields fail to effectively couple with the dominant low-order cogging torque harmonic components in the motor. The introduction of the 5th- and 7th-harmonic magnetic fields may have distorted the air-gap magnetic field distribution to some extent, resulting in an unfavorable modulation effect and underperforming optimization results. This outcome highlights the importance of precisely selecting

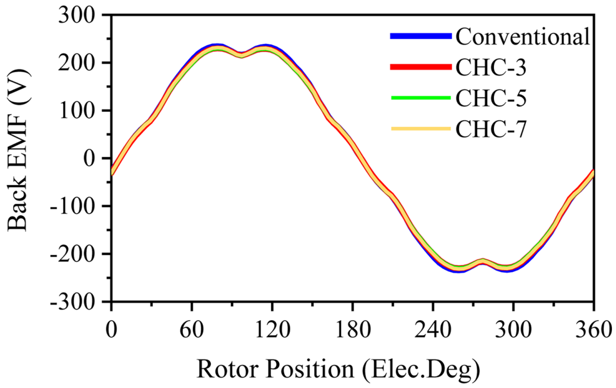

**Fig. 9.** (Color online) Comparison of output no-load back EMF waveforms in Halbach machines with different pole arc trimming structures.

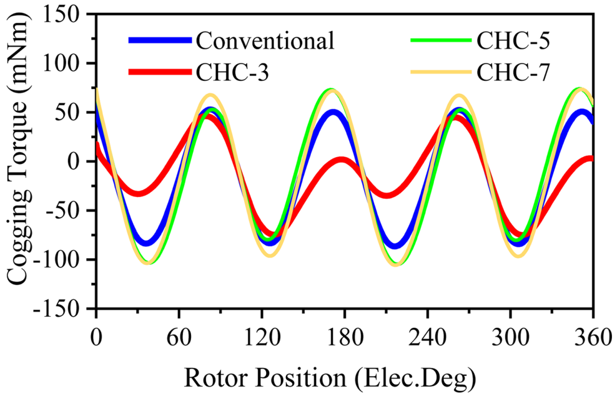

**Fig. 10.** (Color online) Comparison of output cogging torque waveforms in Halbach machines with different pole arc trimming structures.

matching harmonic orders for cogging correction, which must be tailored to specific motor topologies.

Regarding the energy coupling mechanisms in torque ripple, torque pulsations primarily arise from the interaction between the spatial harmonics of the air gap magnetic field and the harmonic components of the armature current's magnetic potential. For integer-slot windings, although the 3rd-harmonic magnetic field is not manifested in the three-phase line EMF, it interacts with specific harmonics of the armature reaction field to generate pulsating torque components at specific frequencies. In contrast, higher-order harmonics, such as the 5th and 7th, typically exhibit lower amplitudes, and the torque ripple generated by their coupling with the armature magnetic field occurs at higher orders and often carries weaker energy. Therefore, prioritizing the suppression of the 3rd harmonic with the largest amplitude and the greatest impact achieves the optimal gain, yielding the greatest improvement in torque smoothness with minimal alterations of the permanent magnet shape (i.e., minimal potential loss of the fundamental magnetic flux).

Thus, in Halbach machines, the injection of the 3rd-harmonic component for the cosine-shaped pole-arc modification is an optimal strategy that maximizes energy coupling while deeming manufacturing feasible. This approach precisely targets the primary low-order harmonic disturbances that inevitably arise from manufacturing imperfections, thereby achieving a more significant and fundamental torque ripple suppression than injecting 5th- or 7th-harmonic components.

The results of this study indicate that adopting the magnetic pole arc-trimming strategy based on the cosine function and incorporating the 3rd harmonic can significantly reduce the torque ripple amplitude while maintaining essentially the same torque output, representing a practical design approach for optimizing the high performance of Halbach array permanent magnet machines.

## 5. Conclusion

This paper systematically investigates the mechanism by which cosine-based high-order harmonic injection trimming methods influence the air gap magnetic flux density and torque characteristics of Halbach array permanent magnet synchronous machines, focusing on the optimization of magnet pole arc trimming. Simulation results were compared across different trimming schemes (untrimmed, CHC-3, CHC-5, and CHC-7), comprehensively revealing the underlying mechanisms and differences in the performance of various high-order harmonic modifications. Among the studied trimming schemes, the CHC-3 scheme demonstrated superior torque ripple suppression compared to CHC-5 and CHC-7, reducing the generated torque ripple by ~20.658%, while the average torque was only reduced by ~1.540%. This demonstrates that the CHC-3 scheme can significantly suppress torque ripple in Halbach machines without affecting the torque output capability. The primary innovations and theoretical contributions of this study can be summarized as follows:

A novel cosine pole-arc trimming method incorporating higher-order harmonic injection was proposed. By introducing the cosine-based parametric shaping strategy in Halbach machines, shaping curves were systematically constructed via tunable harmonic injection.

Crucially, the parametric curve design was applied only at the pole edge, eliminating the need for an additional magnet or quantity while preserving the original magnetization direction and mounting structure, and employs relatively simple shaping curve functions. This approach achieves an excellent trade-off between manufacturing feasibility, performance enhancement, and design flexibility.

By systematically analyzing and comparing the proposed CHC-3, CHC-5, and CHC-7 schemes, a three-dimensional optimization evaluation system, a Performance-Complexity-Accuracy triad was proposed to comprehensively assess their effectiveness in suppressing torque ripple, maintaining the torque output almost unchanged, and achieving a performance-complexity balance.

Nevertheless, several issues warrant further exploration in spite of the detailed study. For instance, the effects of three-dimensional magnetic fields were not fully considered, and the conducted research primarily relied on a two-dimensional finite element model, neglecting the leakage of the axial magnetic flux and end effects [21]. Future work should establish a three-dimensional model to verify the magnetic field variations and loss characteristics in the end regions resulting from the proposed modification. The automatic optimization of harmonic parameters has yet to be developed. Currently, the amplitude and phase of harmonics are primarily determined by manual parameter tuning. Subsequent work should integrate genetic algorithms [22], particle swarm optimization [23], or Bayesian optimization algorithms [24] to achieve multi-objective automatic optimization. The derived conclusions and applied methods can be primarily applied to conventional surface-mounted machines and still exhibit limitations and shortcomings: achieving a desired air gap magnetic flux density through variations in the thickness of permanent magnets or excessive adjustment of the air gap length results in overly complex-correction function designs.

In summary, this research holds significant theoretical and practical value for the development and optimization of high-end drive systems.

## Acknowledgment

This work was supported by the National Natural Science Foundation of China (52307061), the national Science Research Program of Jiangsu Colleges and Universities under Grant (24KJA470005), the Postgraduate Research & Practice Innovation Program of Jiangsu Province (SJCX24_2005).

## References

[1] T. Ouyang, S. Jin, X. Xie, Y. Gong, and Z. Zhang, IEEE Trans. Transp. Electrific. **11**, 12647 (2025).
[2] S. H. Kang, H. S. Kim, Y. S. Hwang, and B. K. Lee, IEEE Trans. Power Electron. **40**, 17384 (2025).
[3] Y. Yan, H. Wang, L. Wang, Z. Wang, P. Xu, J. Wan, Y. Wang, X. Duan, P. Lian, and C. Wang, IEEE Trans. Antennas Propag. **73**, 9798 (2025).
[4] Z. Zhao, C. Hu, S. Wu, Z. Wang, and Y. Zhu, IEEE Trans. Ind. Electron. **72**, 9841 (2025).
[5] X. Zhang, J. Zhang, D. Zeng, J. Zhao, B. Xu, and C. Zhang, IEEE/ASME Trans. Mechatronics **29**, 1240 (2024).
[6] Y. Zhou, X. Zhong, H. Diao, B. Ma, F. Tang, X. Fu, P. Lai, H. Wang, J. Liu, X. Chen, G. Lu, H. Chen, and X. Yang, IEEE Trans. Device Mater. Rel. **25**, 966 (2025).
[7] S. Fan, J. Guo, Y. Zeng, D. Li, and S. Ma, CSEE J. Power Energy Syst. **11**, 2535 (2025).
[8] P. Lv, N. Wang, X. Su, Z. Shang, C. Zhang, and J. Fu, IEEE Trans. Magn. **61**, 1 (2025).
[9] F. Li, K. Wang, F. Huang, Z. Liu, Y. Guo, J. Li, and H. Ge, IEEE Trans. Ind. Appl. **61**, 9232 (2025).
[10] P. Vats and B. Singh, IEEE Trans. Plasma Sci. **53**, 1630 (2025).
[11] Q. Lv and S. Fang, IEEE Trans. Transp. Electrif. **11**, 12494 (2025).
[12] H. Qiu and K. Wang, IEEE Trans. Power Electron. **40**, 17703 (2025).
[13] J. Zhu, H. Wang, Y. Shen, H. Yamamoto, R. Kajitani, and C. H. T. Lee, IEEE Trans. Transp. Electrif. **11**, 11199 (2025).
[14] N. Shrivastava, S. Sashidhar, and B. Subudhi, IEEE Trans. Magn. **61**, 1 (2025).
[15] K.-C. Liu, S.-G. Lin, K.-Y. Peng, and J.-Y. Chang, IEEE Trans. Magn. **61**, 1 (2025).
[16] J. Qi, Z. Zhu, L. Yan, G. W. Jewell, C. Gan, Y. Ren, S. Brockway, and C. Hilton, IEEE Trans. Ind. Appl. **58**, 3511 (2022).
[17] B. Guo, F. Peng, Z. D. Khedda, F. Dubas, and Y. Huang, IEEE Trans. Transp. Electrif. **9**, 3085 (2023).
[18] J. Qi, Z. Q. Zhu, L. Yan, G. W. Jewell, C. Gan, Y. Ren, S. Brockway, and C. Hilton, IEEE Trans. Ind. Appl. **58**, 3545 (2022).
[19] L. Qian, L. Sun, K. Wang, and M. Tong, IEEE Tran. Ind. Electron. **70**, 6551 (2023).
[20] Y. Ji, Y. Li, and Q. Lu, IEEE Trans. Ind. Appl. **61**, 9159 (2025).
[21] R. Mellerud, C. Hartmann, C. L. Klop, R. Dorget, and J. K. Nøland, IEEE Trans. Appl. Supercond. **35**, 1 (2025).
[22] J. Yang, Y. Song, J. Tang, W. Ding, Z. Lei, and S. Gao, IEEE/CAA J. Autom. Sinica **12**, 2314 (2025).
[23] K. Bojappa and J. Lee, IEEE/CAA J. Autom. Sinica **12**, 1762 (2025).
[24] H. Wang, X. Li, L. Zheng, A. Bhaumik, and P. Vadakkepat, IEEE Robot. Autom. Lett. **10**, 11538 (2025).